ISSN 0915-633X

NATIONAL INSTITUTE FOR FUSION SCIENCE

Optimization of the Visible CXRS Measurements of TESPEL Diagnostics in LHD

V.Yu. Sergeev, R.K. Janev, M.J. Rakovic, S. Zou, N. Tamura,
K.V. Khlopenkov and S. Sudo

(Received - July 5, 2001)

NIFS-710 Aug. 2001

RESEARCH REPORT
NIFS Series

TOKI, JAPAN

Optimization of the Visible CXRS Measurements of TESPEL Diagnostics in LHD

V.Yu. Sergeev[1,2], R.K. Janev[1,3] M.J. Rakovic[4], S. Zou[1,5], N. Tamura[1,5], K.V. Khlopenkov[1]
and S. Sudo[1]

[1] *National Institute for Fusion Science,Toki, Japan,*
[2] *State Technical University,St. Petersburg, Russia,*
[3] *Macedonian Academy of Sciences and Arts, Skopje, Macedonia,*
[4] *Oak Ridge National Laboratory ,Oak Ridge, USA,*
[5] *The Graduate University for Advanced Studies, Hayama, Japan.*

Abstract

A model for calculations of Charge eXchange Recombination (CXR) signals of impurity nuclei injected in high temperature plasma has been developed. For that purpose, the simplified collisional-radiative model for calculations of CXR signal and the corona equilibrium set of equations for ionization balance were solved taking into account the main physical processes involved. Scaling laws of partial CX cross sections with respect to both principal and angular quantum numbers of captured electron have been established on the basis of the results of Classical Trajectory Monte Carlo (CTMC) calculations.

The CXR signals for a Li tracer in TESPEL experiments on LHD and CHS machines have been calculated. The difference of about two orders of magnitude in the calculated signals is due to the difference of both NBI neutral flux density and capture-radiation cross-sections and explains the lack of Li^{3+} CXR signals in the measurements on LHD.

Calculations of the CXR signals for various injected impurities have been performed for LHD conditions. The operational limits of the use of TESPEL diagnostics in the visible spectral range on LHD have been determined. For T_e=1-2 keV (P_{NBI} = 3 MW) and N_e=(2-5)$\cdot 10^{13}$ cm^{-3}, injection of F, Mg and Al as tracer materials is proposed.

Keywords: diagnostics, impurity transport, pellet, charge exchange, radiation

1. Introduction

The Tracer Encapsulated Solid Pellet (TESPEL) injection method has been recently proposed for diagnostics of impurity transport of the core toroidal plasmas [1]. The basic idea of this method is illustrated on example of the TESPEL diagnostics setup developed for LHD and shown in Fig. 1.

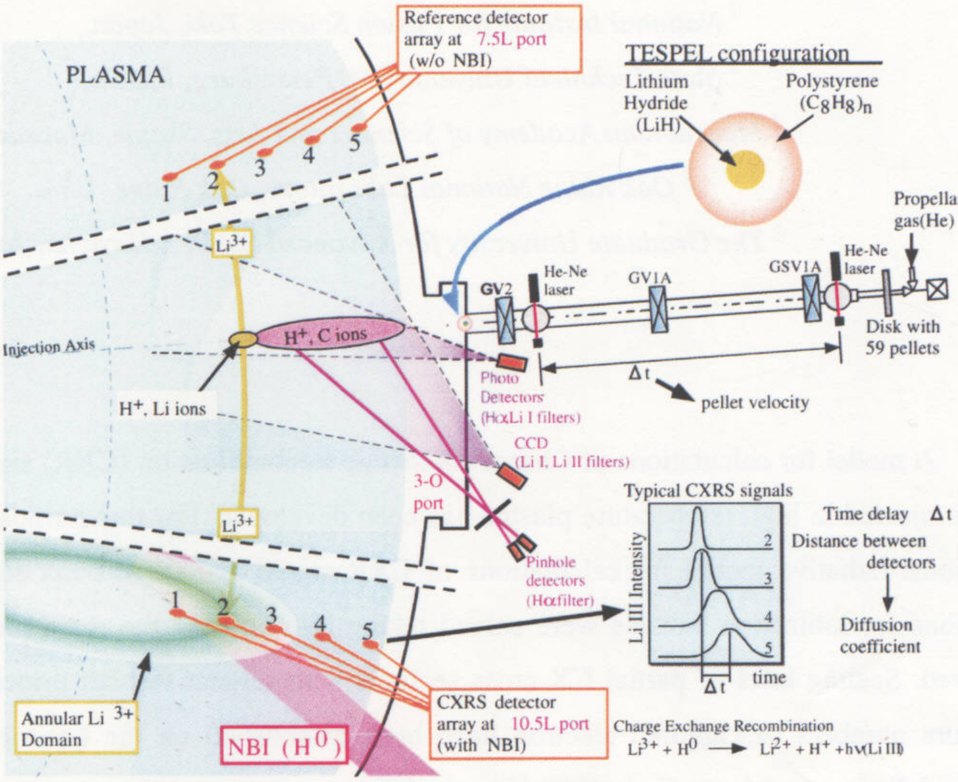

Fig. 1. *Setup of TESPEL diagnostics in LHD.*

A solid impurity material (tracer) is encapsulated in the outer layer of polystyrene (shell) and is accelerated in the direction of plasma core by pellet injector with a He propellant gas. The ablating pellet deposits in the plasma firstly its shell material and then the tracer material (LiH in our example) in a narrow region (order of several cm) of the plasma core. After toroidal symmetrization and complete ionization of the tracer material, a Li^{3+} annular domain is created. The radial behavior of this localized domain can be measured by observation of CXR emission intensity due to CX reaction of the injected impurity nuclei I^Z (of nuclear charge Z) with the neutral beam injection (NBI) hydrogen atoms (assumed to be in their ground state)

$$I^{Z+} + H_{1s} \Rightarrow I_{nl}^{(Z-1)+} + H^{+} \qquad (1)$$

where n and l are the principal and orbital angular quantum numbers of the captured electron on the ion. For ions with charge Z, the electron capture takes place preferentially on excited energy levels with $n \approx Z$. For $Z \geq 2$, these are the excited product ion levels that radiate and the emission of which gives the basis for the CXR – based spectroscopy (CXRS) diagnostics of plasma impurities (and other plasma parameters).

The CXR signal is measured within certain visible spectral range. Therefore, perturbation of the signal caused by continuum radiation is possible mainly due to ablatant created by the shell material. The amount of tracer material is about two orders of magnitude less than the amount of shell particles. Estimations show that the input of tracer material in the perturbation of continuum radiation can be neglected up to the trace charge values of $Z \approx$ 17-18. Besides, a background (reference) emission can appear due to the charge exchange between fully ionized ions and thermal neutrals which come from the plasma edge where the ion temperature is low [2]. For these reasons, the CXRS system developed for measurements of plasma poloidal rotation [2] is used. In this system, the CXRS detector array in the NBI port is arranged together with the reference detector array that has geometry identical to the CXRS detectors in the port without NBI. Signals from the detectors via optical fibers are transferred to entrance of the set of photo-multipliers. These photo-multipliers are equipped by sets of interference filters that provide measurements of a narrow specific spectral range (~ 1 nm) containing the line intensity of H-like ions of the injected impurity. Thus, subtraction of the reference signals from the CXR detector signals results in pure CXR signals due to reaction (1) that is schematically shown in Fig. 1. Measuring a time interval Δt between maximums of CXR signals with a radial Δr displacement, one can derive the effective diffusion coefficient of impurity averaged over the radial range Δr.

The described approach has been successfully used for Li^{3+} transport studies in TESPEL experiments with LiH tracer on CHS [3]. A sample of the CXRS and reference signals measured in these experiments is shown in Fig. 2a. It is seen that a fairly well pronounced difference of the signals before and after the pellet injection is observed, that has been used for the subsequent signal subtraction. For comparison, the similar signals measured in LHD TESPEL experiments with LiH tracer are shown in Fig. 2b. Unfortunately, no detectable difference has been observed in that case.

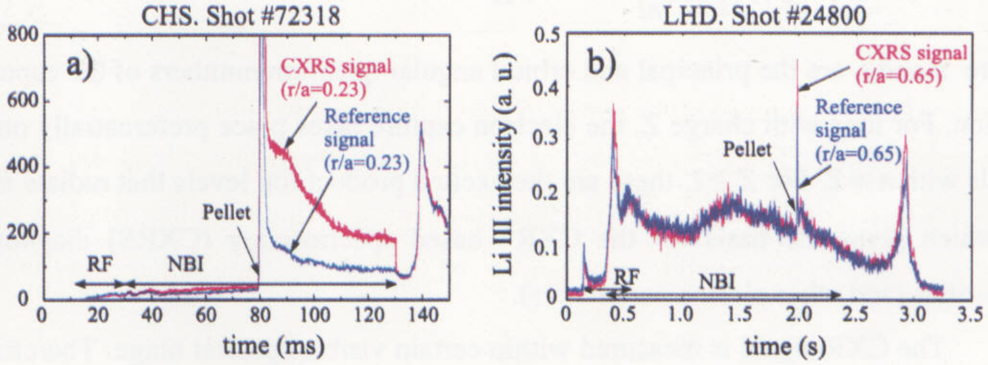

Fig. 2. *Temporal behavior of LiIII radiation intensity (450±0.5 nm) in TESPEL experiments on CHS (a) with E_{NBI} = 36 keV and on LHD (b) with E_{NBI} = 150 keV.*

The purpose of the present paper is to explain the lack of CXR Li^{3+} signal in LHD TESPEL experiments and to determine the operational limits of the TESPEL CXRS diagnostics in the visible spectral range for the study of impurity transport in LHD.

2. General remarks

The key parameter of the problem considered is the cross-section of the reaction (1). In Fig. 3 the reduced total CX cross-section σ^{CXtot}/Z versus the reduced NBI energy $E/Z^{3/7}$ taken from Ref. [4] is shown. The arrows in the figure indicate the conditions for different energy E of NBI and Z of tracer material corresponding to the CHS (E = 36 keV) and LHD (E = 150 keV) TESPEL experiments. It can be seen that the CX total cross-section drastically depends on E and Z. For a Li tracer, the σ^{CXtot} value for CHS is 30 times larger than that for LHD NBI energy. At the fixed energy of NBI in LHD, one should move to higher Z of tracer material (see points for F, Si, Ti shown in Fig. 3) in order to reach the reduced energy region of high reduced CX cross sections.

Increase of the tracer material charge leads to additional requirements. Namely, the ionization of tracer atom can be incomplete at a given electron temperature T_e. Hence, the nuclei density N_Z can differ from the N_{imp} density of the injected impurity by a factor equal to the ionization degree $\alpha_Z = N_Z/N_{imp}$. A CXR signal decreases with decreasing of the nuclei density that may limit observations. Another limitation arises from the requirement that the time τ_{ion} of complete ionization of the injected impurity has to be significantly smaller than the characteristic diffusion time τ_{diff}. For light material like Li, relationships

$$\alpha_Z \approx 1, \qquad \tau_{ion} << \tau_{diff} \tag{2}$$

are easily fulfilled. For higher Z tracers, however, these conditions may be violated and the ionization process of these impurity ions has to be taken into consideration.

Apparatus of the TESPEL diagnostics on LHD has been developed for the visible spectral range. It is well known that only transitions with a change of the principal quantum number n by one ($\Delta n = 1$) can provide wavelengths of fairly high-Z ion radiation in the visible domain. For the radiation in the visible spectral range, these two quantities are related to each other by the following simple relation

$$n_v = 2.2 \cdot Z^{2/3} \tag{3}$$

For instance, the radiation due to electron transition from $n_v = 17$ to n_v-1=16 lies in the visible spectral range only if $Z \cong 22$ (i.e. the tracer has to be titanium, or an element with a close nuclear charge). The relation (3) indicates that when using high-Z tracer elements to have large total CX cross sections, one has to use the radiation from the high-n levels in order to stay within the visible spectral range. For the collision energies above 100 keV the total electron capture cross section is distributed among many quantum levels of the product ion, resulting in relatively small partial n-CX cross sections, especially for the higher n- values of the distribution.

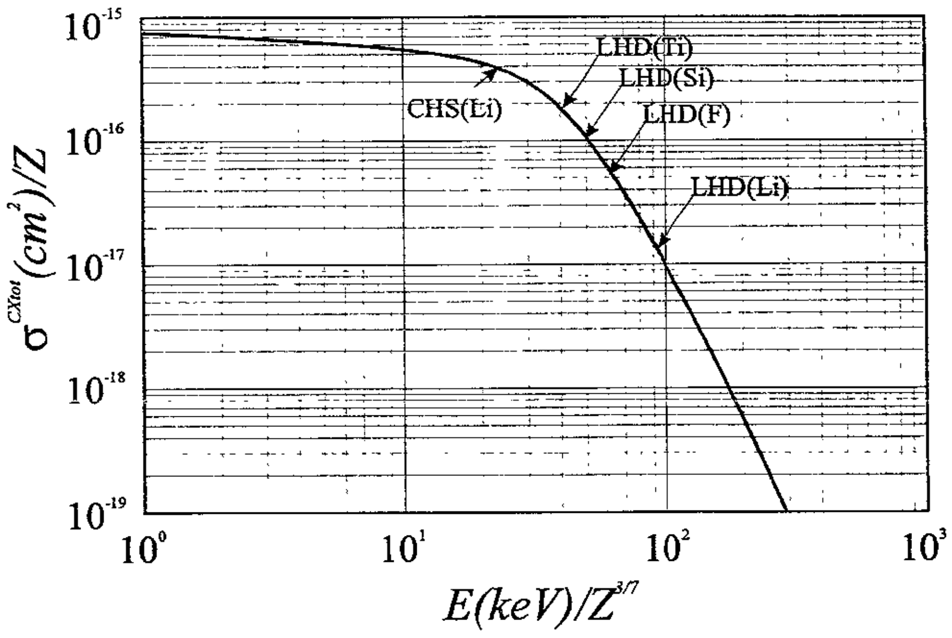

Fig. 3. *The reduced total* σ^{CXtot}/Z *CX cross-section of impurity nuclei with charge Z versus the reduced NBI energy* $E/Z^{3/7}$.

Therefore, although the total CX cross-section increases with Z, it does not automatically guarantees large *n*-partial cross-section to n_v. Moreover, the radiation takes place due to transitions between given initial and final *n,l* –states, which means that the partial *n*-CX cross section has to be distributed among all the *n,l*-substates within a given *n* - energy level, which further reduces the portion of the total cross section that contributes to the CXR signal. Therefore, one should consider the population of the specific sublevels *n,l* very carefully, with inclusion not only the CX process (1) but also all other processes contributing to the population and destruction of the radiating *n,l* sublevel.

3. Model

The consideration of a wide range of charges and varieties of injected impurities with the purpose of optimization of the CXR signal (with respect to the optimal choice of tracer impurity for the given range of LHD plasma parameters and given beam energy) had required to simplify the collisional-radiative (CR) set of equations for calculation of the CXR signal, as well as the corona equilibrium (CE) set of equations for the ionization balance, in order to evaluate the conditions (2).

3.1. Calculation of CXRS signal.

An excited state of an H-like ion in high-temperature plasmas can be populated by radiative recombination with a plasma electron, by charge exchange of the parent nuclei (on the beam atoms), by radiative decay and collisional de-excitation of higher states and collisional excitation of lower states. It can be depopulated by radiative decay and collisional de-excitation to lower states and by collisional ionization.

To calculate CXR signal, the set of CR equations was simplified by taking into account the following dominant processes that populate the '*nl*' states of hydrogen-like impurity ions with density N_{nl}^{Z-1}:

1. CX reaction (1) with partial CX cross section σ_{nl}^{CX} to specific '*nl*' state with given principal *n* and angular *l* quantum numbers.
2. Radiative decay cascade from all levels with n'--> *n* to the level *n*.
3. Radiative decay transitions from the level *n* to all levels with n'<-- *n*.

It is shown in the Appendix that for large *Z* and *n* of interest here, the processes of radiative recombination of nuclei, excitation, de-excitation and ionization of H-like ions of injected impurity are negligible in comparison with the processes listed above. Thus, a set of equations for population of the H-like ion density N_{nl}^{Z-1} to the specific state *nl* is

$$\frac{dN_{nl}^{Z-1}}{dt} = N^Z N_H v_H \sigma_{nl}^{CX} + \sum_{n'>n,l'} N_{n'l'}^{Z-1} A_{n'l',nl}^{Z-1} - N_{nl}^{Z-1} \sum_{n'<n,l'} A_{nl,n'l'}^{Z-1} \qquad (4)$$

Here, N^Z is the density of impurity nuclei, $N_H\ v_H$ is the flux of NBI atoms, $l' = l \pm 1$ (following from the selection rule for dipole allowed transitions), $A_{nl,n'l'}^{Z-1}$ is the transition probability for spontaneous radiative decay from the *nl* to $n'l'$ state of H-like ions.

The photon volumetric source of CX reaction in the visible spectral range is due to the transitions $nl,(n-1)l'$ only,

$$\frac{dI_{nl,(n-1)l'}^{Z-1}}{dV} = \frac{1}{4p} N_{nl}^{Z-1}\left(A_{nl,(n-1)(l+1)}^{Z-1} + A_{nl,(n-1)(l-1)}^{Z-1} \right) \text{ [photons/m}^3\text{/s/strd]} \qquad (5)$$

The solution of equations (4) was obtained by using approach described in Ref. [5]. Thus, for steady state condition t >> 1/min(A_{nl}^{Z-1}) from the set of equations (4) one can obtain

$$N_{nl}^{Z-1} = N^Z N_H v_H \left(\sigma_{nl}^{CX} + \sum_{n'>n} C_{n',n} \sigma_{n',l}^{CX} \right) \Big/ \sum_{n'<n} A_{nl,n'l'}^{Z-1}, \qquad (6)$$

where $C_{n'n}$ is the cascade matrix from all levels $n' > n$ calculated in Ref. [5]. Substituting Eq. (6) into Eq. (7), and making summation over the whole range of the angular quantum number *l*, we have

$$\frac{dI_{n,(n-1)}^{Z-1}}{dV} = \frac{1}{4p} N^Z N_H v_H \left\langle \sigma_{n,(n-1)}^{CX} \right\rangle \qquad \text{[photons/m}^3\text{/s/strd]}, \qquad (7)$$

where $\left\langle \sigma_{n,(n-1)}^{CX} \right\rangle$ is the capture-radiation cross section for the transition $n \rightarrow n-1$,

$$\left\langle \sigma_{n,(n-1)}^{CX} \right\rangle = \sum_{l=0}^{n-1} \left(\sigma_{nl}^{CX} + \sum_{n'>n} C_{n',n} \sigma_{n',l}^{CX} \right) \cdot P_{nl,(n-1)l'}, \qquad (8)$$

and $P_{nl,(n-1)l'}$ is the radiation probability that is the ratio of A_{nl}^{Z-1} decay probabilities for the transitions $nl \Rightarrow (n\text{-}1)l'$ to the total probability of radiative decay of the level n:

$$P_{nl,(n-1)l'} = \frac{A_{nl,(n-1)(l+1)}^{Z-1} + A_{nl,(n-1)(l-1)}^{Z-1}}{\sum\limits_{n'<n} A_{nl,n'l'}^{Z-1}} , \tag{9}$$

To calculate the radiation photon flux measured in experiments by a detector with a detection area S_d and a radial position R_d, the volumetric source of CX photon flux emission (7) has to be integrated over the whole observation volume V_{em}

$$I_{n,n-1}^{Z-1} = \int\limits_{V_{em}} \frac{S_d}{4\pi R_d^2} N^Z N_H v_H \left\langle \sigma_{n,(n-1)}^{CX} \right\rangle dv \qquad \text{[photons/s]}, \tag{10}$$

One can see from Eq.(10) that for fixed NBI energy and power, and for a given geometry of TESPEL experiments, CXR signal is proportional to the $\left\langle \sigma_{n,(n-1)}^{CX} \right\rangle$ capture-radiation cross-section multiplied on the density N^Z of the nuclei. From a methodological point of view, we should keep the amount of injected impurity on a fairly low level. Therefore, key parameters are the dependencies of σ_{nl}^{CX} partial cross-section and $P_{nl,(n-1)l'}$ radiation probability for H-like atomic systems on the n, l quantum numbers (see Eqs. (8,9)).

3.2. Partial CX cross-sections and radiation probability.

The n- and n,l- partial CX cross-sections for 150 keV NBI energy in LHD were calculated for the fully stripped ions with Z=3, 6, 9, 12, 14, 18, 22 by using the CTMC code. Since the calculations are highly time-consuming, the following scaling fit-functions for σ_{nl}^{CX} and $\sigma_n^{CX} = \sum\limits_{l=0}^{n-1} \sigma_{nl}^{CX}$ were devised:

$$\sigma_n^{CX}(n,Z) = 1.1 \cdot 10^{-17} Z^{3/2} \frac{\exp\left(-\dfrac{1.35}{(n/Z^{0.815})^{2.3}} \right)}{(n/Z^{0.815})^3} \tag{11}$$

$$\sigma^{CX}_{n_\nu}(l,Z)=\sigma^{CX}_{n}(n_\nu,Z)\frac{9.5}{Z^{0.75}}\left(\frac{l^{4}}{Z}+\frac{l}{8Z}\right)exp\left(-\left(\frac{1.431}{Z}\left(l+310^{-6}Z^{3}\right)\right)^{8+\frac{Z^{2.5}}{200}}\right) \qquad (12)$$

The results of CTMC calculations and those produced by the scaling functions (11,12) for some Z –ions from the Z=3-22 range are shown in Fig. 4. For the Z = 6-22 range, the principal quantum numbers n_ν for the visible domain are shown by the hatched area in Fig. 4a together with a vertical segment for n_ν corresponding to the Li- tracer material. One can see that the

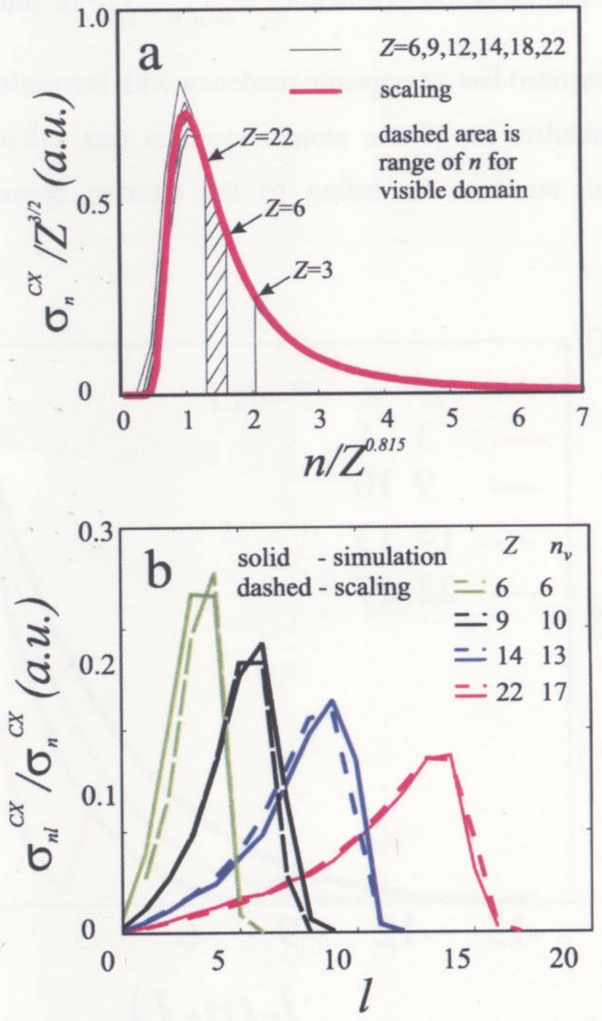

Fig. 4. *Dependencies of partial total* σ^{CX}_{n} *(a) and* $\sigma^{CX}_{n_\nu l}$ *(b) versus the quantum numbers n, l.*

partial cross-sections σ_n^{CX} corresponding to the visible domain increase with increasing Z and their values are not far from the region of the maximum values.

It is seen from Fig. 4b that with increasing Z the σ_{nl}^{CX} dependencies have a tendency to be closer to the statistical distribution $\sigma_{nl}^{CX}/\sigma_n^{CX} = (2l+1)/n^2$ over *l*. It seems that the *n,l* – distribution of captured electrons is closer to a situation when the "string mixing" of Stark states due to the rotation of the internuclear axis [6] takes place as the population mechanism of different *n,l*-substates in reaction (1). However, for light Z materials the σ_{nl}^{CX} maximum over *l* shifts to the low *l* values (the case of "weak mixing" [6]) and this situation is unfavorable if one takes into account that the radiation probability $P_{nl,(n-1)l'}$ (a multiplier in Eq. (8) for the capture-radiation cross-section) has an opposite tendency with increasing *l*, as shown below.

A radiation probability for H-like atomic systems was calculated for different Z-ions versus the *n, l* quantum numbers according to the Cordon approach [7]. The calculated

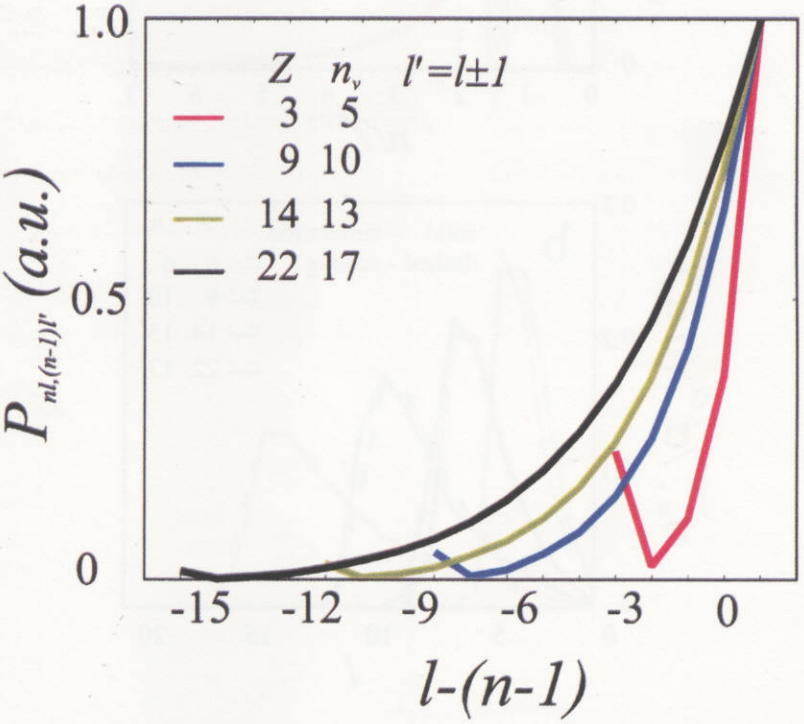

Fig. 5. *The radiative transition probability* $P_{nl,(n-1)l'}$ *from the nl-substate to the (n-1)l′substates versus the angular quantum number l.*

$P_{nl,(n-1)l'}$ dependencies on the angular quantum number l, subtracted by their maximal values $(n-1)$ for the given n, are shown in Fig. 5. The values of n_v for different Z in Fig. 5 correspond to the transitions in the visible domain (Eq. (3)).

3.3. Ionization balance of high Z ions.

The ionization degrees α_Z have been calculated for a wide Z- range using the simplified CE set of equations (13). The number of injected nuclei has to be very large (preferably close to amount of injected atoms) for a CXR measurement. It is well known that the ionization degree becomes large for temperatures $T_e \geq I_{ion}$ with I_{ion} being ionization potential of H-like ions. Therefore, one can take that the densities of all states, beginning from the Li-like one, are zero, which is a quite acceptable approximation for the temperature range of interest here. This gives the well-known CE result

$$N^Z/N^{Z-1} = S^{Z-1}/R^Z, \qquad N^q \equiv 0, \; q = Z-3, Z-4, \ldots..0, \tag{13}$$

where S^{Z-1} and R^Z are the effective ionization and recombination rate coefficients of the indicated ions. Thus, only the nuclei, H- and He-like ions were taken into account in our model. The ionization rate coefficients presented in the Appendix were calculated for the ground states $(n = 1)$ only, since due to the large radiative decay probabilities a small population of higher principal quantum numbers is expected. The results of calculations of effective ionization rate coefficient of H-like ions, performed within the CR model [5], confirm the validity of this approach. The rate coefficients for other processes, needed in the ionization balance calculations and used in the present paper, are given in the Appendix. Because of small values of the ratio $N_H/N_e = (1\text{-}3)\cdot 10^{-6}$, we have neglected the CX recombination term in the ionization balance equations. In that case, the calculation of α_Z becomes independent of the electron density.

To validate our simplified calculations of α_Z, we compare the obtained results with those obtained using the MIST impurity transport code [9], in which all ionization states are taken into account in Eqs. (13). The comparison is shown in Fig. 6. It seen that the simplified model slightly underestimates the α_Z values, and the difference increases with increasing Z and decreasing T_e. However, these discrepancies are not larger than 10-15% even for high Z material like Ti at T_e =10 keV.

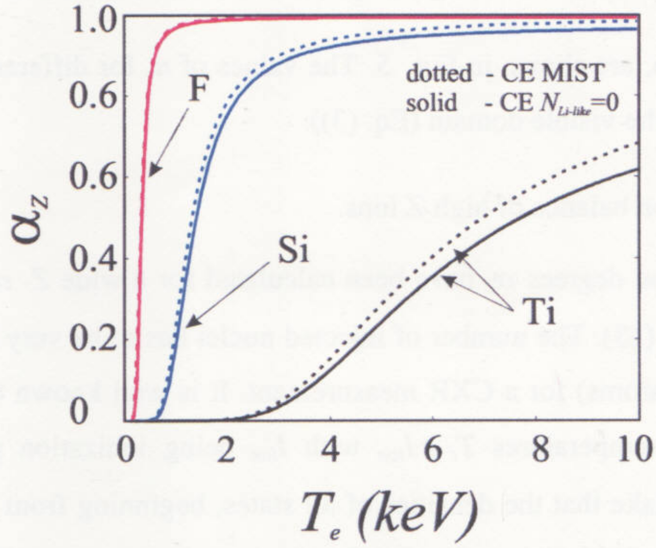

Fig. 6. *Complete ionization degree α_Z versus electron temperature calculated by the simplified model (solid curves) and by MIST code (dotted curves) for F, Si, Ti.*

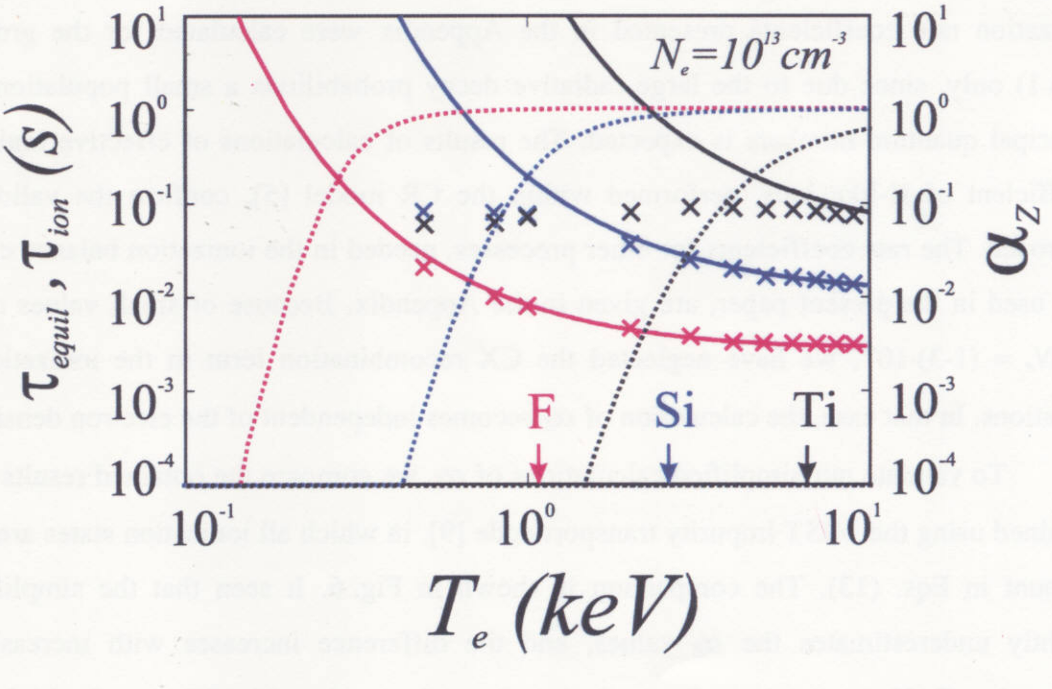

Fig. 7. *Complete ionization time τ_{ion} calculated by the simplified model (solid curves) and equilibrium time τ_{equil} by MIST code (crosses) versus electron temperature, for F, Si, Ti. Dotted curves are α_Z dependencies on T_e from Fig. 6. Arrows to x-axis show ionization potentials of H-like ions of impurities shown.*

In order to estimate the time needed for complete ionization τ_{ion}, we used the fact that the ionization potentials of H- an He-like ions of injected impurities are close to each other and these values are much larger than the ionization potentials of lower ionization states. Thus, τ_{ion} can be estimated as the sum of ionization times of H- an He-like ions for the temperature range of interest, $T_e \geq I_{ion}$. Using the MIST code, we have calculated the time τ_{equil} needed to reach the ionization equilibrium of an impurity with charge Z at the given electron temperature T_e. The results of these calculations are shown in Fig. 7 together with the α_Z values from Fig. 6. It can be seen that for temperatures $T_e \geq I_{ion}$, the times τ_{ion} calculated by our CE model are close to τ_{equil} obtained from the MIST code calculations. The decrease of τ_{equil} for temperatures lower than the corresponding ionization potential can be explained by the fact that for these conditions the equilibrium is determined by the lower ionization states, with correspondingly lower ionization times.

4. Results of Calculations and Discussion

4.1. Calculations of CXRS signal for CHS and LHD.

In Fig. 8, the partial CX radiation cross-sections for Li material as a tracer for CHS

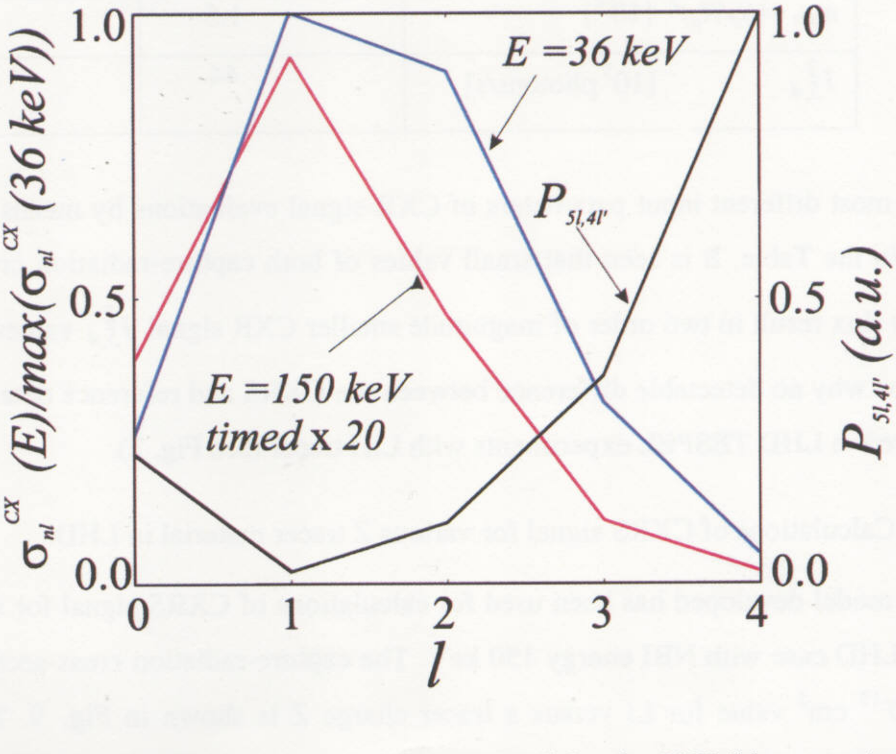

Fig. 8. *Partial CX radiation cross-sections versus l for the CHS (blue curve) and for LHD (red curve). Black curve is l dependence of the radiation probability for H-like Li ion.*

(E_{NBI} = 36 keV) and LHD (E_{NBI} = 150 keV) cases are shown, together with the l dependence of the radiation probability for H-like Li ion. The reasons resulting in the large difference of Li capture-radiation cross sections in these two machines are evident from Fig. 8. There are small absolute values of CX cross-section and unfavorable dependence of the partial cross-section on the angular quantum number l relative to l-dependence of the radiation probability mentioned above. Results of evaluations of CXR signals of Li^{3+} ions for TESPEL experimental conditions on these two machines are presented in Table 1. Here, R_p is pellet radius.

Table 1.

Parameter	CHS	LHD
P_{NBI} [MW]	0.7	3
E_{NBI} [keV]	36	150
S_{NBI} [m^2]	0.016	0.36
$J/e=n_H v_H$ [$10^{17} cm^{-2} s^{-1}$]	5	0.2
$\left\langle \sigma^{CX}_{n,(n-1)} \right\rangle$ [$10^{-17} cm^2$]	1.47	0.047
R_p [mm]	0.025	0.1
$N_Z = N_{Li}$ [$10^9 cm^{-3}$]	5	10
V_{em} [cm^3]	10	60
$\omega_{det} = (S_d/R_d)^2$ [10^{-4}]	1.5	1.0
$I^2_{5,4}$ [10^5 photons/s]	44	0.44

The most different input parameters of CXR signal evaluations by means of Eq. (10) are underlined in the Table. It is seen that small values of both capture-radiation cross-section and NBI density flux result in two order of magnitude smaller CXR signal $I^2_{5,4}$ values for LHD case. This explains why no detectable difference between the CXRS and reference detector signals has been observed in LHD TESPEL experiments with LiH tracer (see Fig. 2).

4.2. Calculations of CXRS signal for various Z tracer material in LHD.

The model developed has been used for calculations of CXRS signal for various Z tracer material in LHD case with NBI energy 150 keV. The capture-radiation cross-section normalized to its $4.7 \cdot 10^{-19}$ cm^2 value for Li versus a tracer charge Z is shown in Fig. 9. The analysis of Fig. 9 confirms the preliminary conclusion made previously on the basis of considerations of

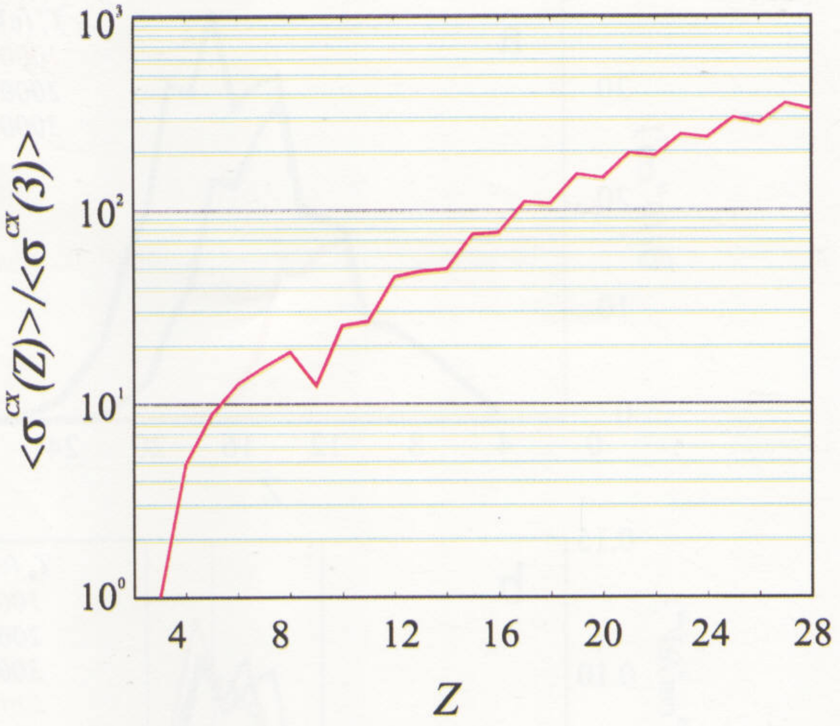

Fig. 9. *Capture-radiation cross-sections normalized at its value for Li versus Z for LHD case with NBI energy 150 keV.*

total cross-section dependence on Z (that one should use higher Z TESPEL injection into LHD plasmas). The evaluated capture-radiation cross-section for $Z \geq 10$ are 30-100 times larger then the one for Li tracer material.

As was mentioned above and can be seen from Eq. (10), at a fixed geometry of the experiment, and NBI energy and power, the CXR signal is proportional to both $\left\langle \sigma^{CX}_{n,(n-1)} \right\rangle$ and the density of injected impurity nuclei, N^Z. The last quantity can differ from the density N_{imp} of injected impurity atoms by (ionization degree) α_Z times. Hence, the CXR signal increases with increasing the product parameter $\Theta = \left\langle \sigma^{CX}_{n,(n-1)} \right\rangle \cdot \alpha_Z$.

The functional dependence of this parameter on Z was calculated using the simplified ionization model and is shown in Fig. 10a for three different electron temperatures. The dependence of parameter Θ on Z has a maximum because $\left\langle \sigma^{CX}_{n,(n-1)} \right\rangle$ increases and α_Z decreases with increasing Z, and it depends on electron temperature. These Z-dependencies can be reduced to one curve by dividing the considered product Θ by $T_e^{3/4}$ and its argument Z by

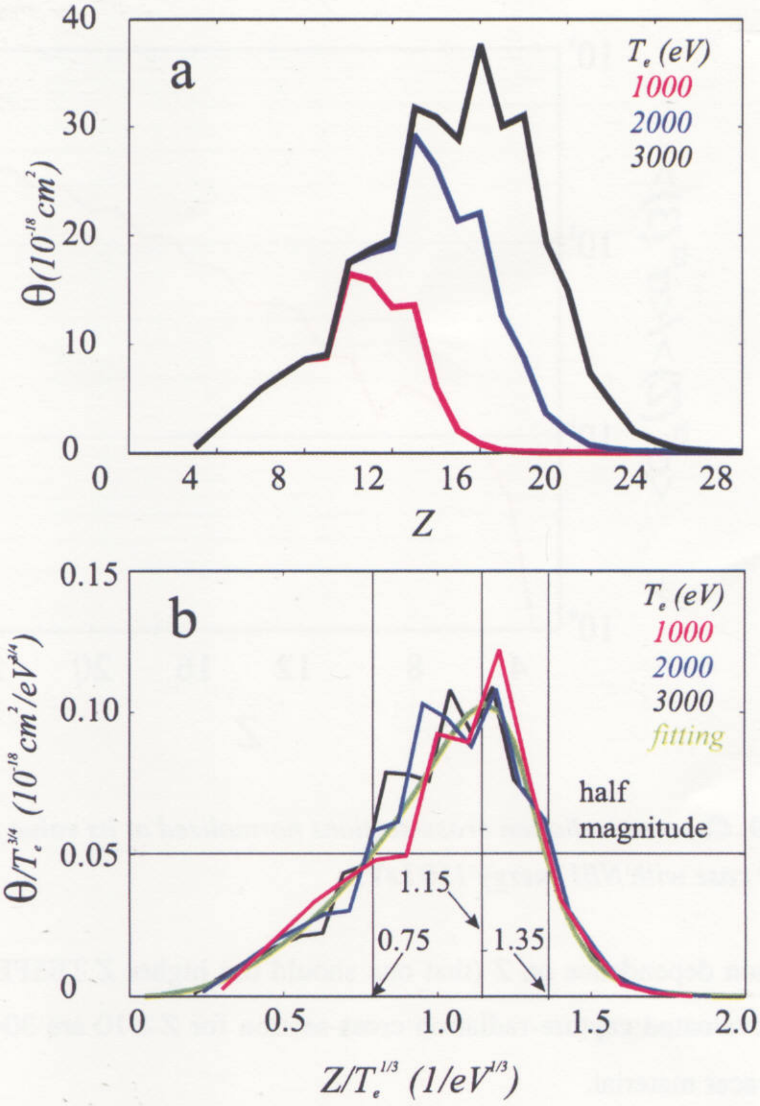

Fig. 10. *Product CXR parameter Θ versus Z for different electron temperatures (a) and reduced product CXR parameters versus reduced Z (b).*

$T_e^{1/3}$. The reduced Θ from Fig. 10a versus reduced tracer charge are shown in Fig. 10b together with their fit $f_{CXR}(x)$:

$$f_{CXR}(x)=\frac{8.5\cdot x^{2.2}}{x^{18}+100} \quad , \quad x=\frac{Z}{T_e^{1/3}(eV)} \tag{14}$$

The observed scaling property of the product Θ allows to derive a simple relationship between the electron temperature and the charge Z_{opt} for which optimal observation conditions of the maximum CXR signal are achieved. In a similar way, one can introduce a range of tracer materials with Z ranging from Z_{min} to Z_{max} by the requirement that the CXR signal level should not be smaller than half of its maximum amplitude. These conditions are shown below

$$Z_{opt} = 1.15 \cdot T_e^{1/3}(eV), \quad Z_{min} = 0.75 \cdot T_e^{1/3}(eV), \quad Z_{max} = 1.35 \cdot T_e^{1/3}(eV) \qquad (15)$$

4.3. Operational limits of TESPEL diagnostics in LHD.

Let us specify the condition (2) by requiring that the complete ionization time τ_{ion} has to be 3 times smaller than the characteristic diffusion time τ_{diff}. For an impurity diffusion coefficient $D = 5 \cdot 10^3$ cm^2/s, and a distance between CXRS detector channels $\Delta r = 20$ cm, τ_{diff} can be estimated as $\tau_{diff} = \Delta r^2/(4 \cdot D) = 20^2/(4 \cdot 5 \cdot 10^3) = 20$ ms. Thus, we have

$$\tau_{ion}(Z, T_e, N_e) = \tau_{diff}/3 \approx 7 \text{ ms} \qquad (16)$$

Finally, the condition (15) for the CXR signal level and the condition (16) for complete

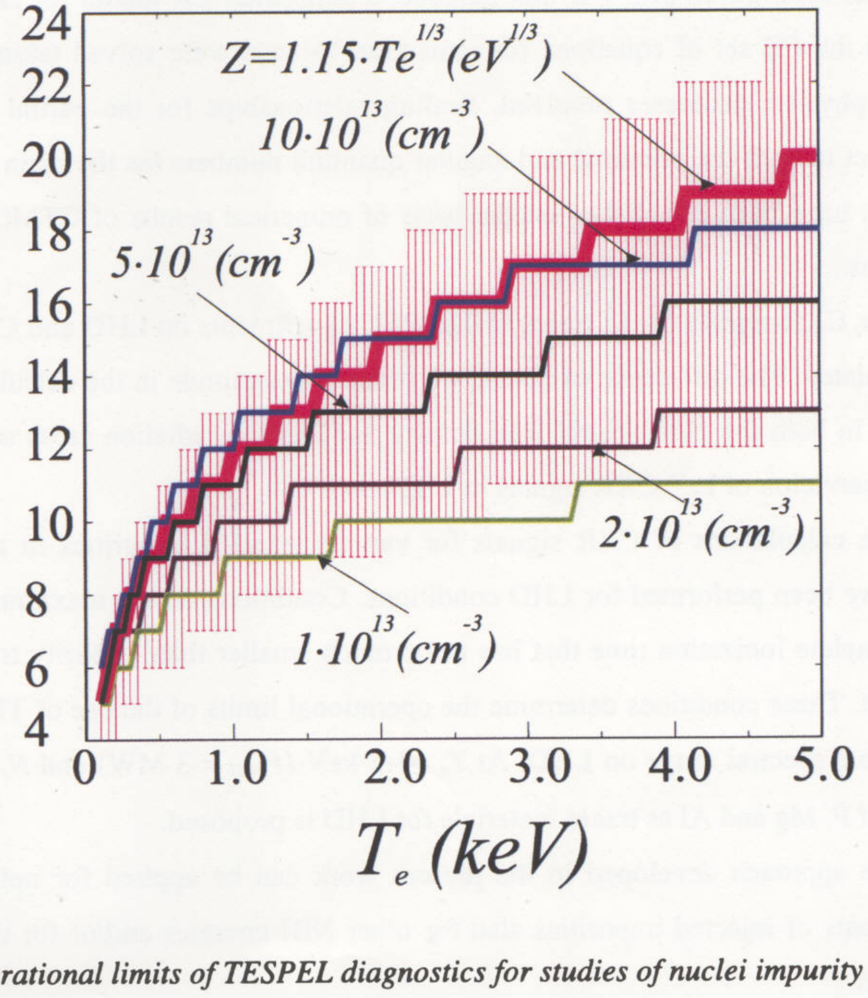

Fig. 11. *Operational limits of TESPEL diagnostics for studies of nuclei impurity transport in LHD machine with NBI energy 150 keV.*

ionization of injected impurity lead to establishment of certain operational limits of TESPEL diagnostics for studies of the fully stripped impurity transport in LHD at the NBI energy of 150 keV. These limits are shown in Fig. 11. The red thick line and error bars represent the equations (15) for Z_{opt} and Z_{min}, Z_{max}, respectively. The conditions (16) are shown by four curves for different electron plasma densities in the range 10^{13}-10^{14} cm^{-3}. The limits shown in Fig. 11 can be easily used for choosing the TESPEL tracer material. The choice should be made for materials with atomic number within the red error bars, preferably closer to the red thick curve corresponding to maximum CXR signal, and below the curve which represents the condition on ionization time for the given electron plasma density. For example, for T_e =1-2 keV (P_{NBI} = 3 MW) and N_e = (2-5)$\cdot10^{13}$ cm^{-3}, injection of F, Mg and Al as a tracer material should be considered as favorable from the point of view of high CXR signals.

5. Conclusions

A model for calculations of CXR signals of impurities injected in high temperature plasmas has been developed. For that purpose, a simplified CR model for calculations of CXR signal and the CE set of equations for ionization balance were solved taking into account the dominant physical processes involved. Scaling relationships for the partial CX cross-sections with respect to both the principal and angular quantum numbers (as the main input parameter in the model) have been established on the basis of numerical results of CTMC CX cross section calculations.

The CXR signals for Li tracer in TESPEL experiments on LHD and CHS machines have been calculated. The difference of about two order of magnitude in the calculated signals due to difference in both the NBI neutral flux density and capture-radiation cross section explains the lack of observation of Li^{3+} CXR signals in LHD.

The calculations of CXR signals for various injected impurities in a high temperature plasma have been performed for LHD conditions. Conditions on the maximum CXR signal and on the complete ionization time that has to be much smaller than impurity transport time, have been found. These conditions determine the operational limits of the use of TESPEL diagnostics in the visible spectral range on LHD. At T_e =1-2 keV (P_{NBI} = 3 MW) and N_e = (2-5)$\cdot10^{13}$ cm^{-3}, injection of F, Mg and Al as tracer materials for LHD is proposed.

The approach developed in the present work can be applied for optimization of CXR measurements of injected impurities also for other NBI energies and/or for the VUV region of observation.

Acknowledgements

Authors thank Dr. H. Funaba for the help with running the MIST code and Dr. T. Kato and Dr. M. Sasao for fruitful discussions. This work was supported by the Japanese Society for Promotion of Science, Grant No L00537.

References

[1] S. Sudo. Diagnostics of Particle Transport by Double-Layer Pellet, Jap. Plasma Fusion Res. **69**, (1993) p. 1349.

[2] K. Ida, S. Kado and Y. Liang. Measurements of poloidal rotation velocity using charge exchange spectroscopy in a large helical device, Rev. Sci. Instrum. **71** (2000) p.2360-2366.

[3] K.V. Khlopenkov. "Impurity Transport Study by means of Tracer-Encapsulated Pellet Injection". Dissertation for the PhD. Department of Fusion Science, The graduate University for Advanced Studies, NIFS, Japan (1998).

[4] R.K. Janev and J.J. Smith. Atomic and Plasma-Material Interaction Data for Fusion, Suppl. J. Nucl. Fus. **4** (1993) p.172.

[5] I.I. Sobelman, L.A. Vainshtein, E.A. Yukov. "Excitation of Atoms and Broadening of Spectral Lines", Springer-Verlag, Berlin, Heidelberg, New York, (1981).

[6] R.K. Janev, L.P. Presnyakov, V.P. Shevelko. "Physics of Highly Charged Ions". Springer-Verlag, Berlin, Heidelberg, New York, Tokyo (1983).

[7] H.A. Bethe and E.E. Salpeter. "Quantum mechanics of one- and two-electron atoms". Springer-Verlag, Berlin, Goettingen, Heidelberg (1957) p. 262.

[8] L.C. Johnson. Astrophys. J. **174** (1972) p.227.

[9] R.A. Hulse. Numeric studies of impurities in fusion plasmas, Fusion technology **3** (1982) pp. 259-274.

[10] T. Kato and E. Asano. Comparison of Recombination Coefficients Given by Empirical Formulas for Ions from Hydrogen through Nickel, Report NIFS-DATA-54 (1999).

[11] V.M. Katkov and V.M. Strakhovenko, Radiative recombination and its application in experiments on electron cooling. Sov. Phys. JETP **48** (1978) pp. 639-643.

[12] Y. Hahn. Improved rate formulas for dielectronic recombination, J. Quant. Spectrosc. Radiat. Transfer **49** (1993) pp. 81-93.

Appendix

Below we estimate different mechanisms of population and de-population of the level with principal quantum number n with the objective to verify the simplification of the CR model done in the model used. Following [5], the spontaneous radiative decay probability A_{n_1,n_0} from level n_1 to level n_0 can be written as

$$A_{n_1,n_0} = A_0 \frac{g_0}{g_1} f_{n_1,n_0} \left(\frac{\Delta E}{Ry} \right)^2 \tag{A.1}$$

where $A_0 = 0.80 \cdot 10^{10}\, sec^{-1}$, f_{n_1,n_0} is the absorption oscillator strength evaluated using [8], $?E = Ry \cdot Z^2 \cdot (1/n_0^2 - 1/n_1^2)$ is the transition energy for threshold energy of excitation from n_1 to n_0, T_e is electron temperature, Ry is Rydberg constant, $g_0 = 2 \cdot n_0^2$ and $g_1 = 2 \cdot n_1^2$ are the statistical weights of states with principal quantum numbers n_0, n_1, respectively.

The values A_{n_1,n_0} of transition from $n_1 = n_v$ to $n_0 = n_v - 1$ should be much larger than those calculated for excitation and de-excitation rate coefficients for this transition. We used the following expression for the excitation rate coefficient (the Van Regemorter formula, see [5])

$$\left\langle v\sigma^{exc}_{n_1,n_0} \right\rangle = 3.2 \cdot 10^{-7} f_{n_1,n_0} \left(\frac{Ry}{\Delta E} \right)^{3/2} \beta^{1/2} exp(-\beta) G(\beta) \qquad [\mathrm{cm}^3/\mathrm{s}], \tag{A.2}$$

and the de-excitation rate coefficient can be obtained from Eq. (A.2) by the detailed balance principle as

$$\left\langle v\sigma^{de-exc}_{n_1,n_0} \right\rangle = 3.2 \cdot 10^{-7} \frac{g_0}{g_1} \langle v \rangle f_{n_1,n_0} \left(\frac{Ry}{\Delta E} \right)^{3/2} \beta^{1/2} G(\beta)\, [\mathrm{cm}^3/\mathrm{s}]. \tag{A.3}$$

Here, β is defined by $\beta = \Delta E / T_e$. The Gaunt factor $G(\beta)$ is a slowly varying function of β, with magnitude of the order of unity:

$$G(\beta) = 0.349 \cdot f(\beta) + 0.0988 + 0.455 \cdot \beta^{\frac{3}{2}} \cdot f(\beta), \tag{A.4}$$

where the function f is taken from [6]

$$f(\beta) = -exp(\beta) Ei(-\beta) \approx ln\left(1 + \frac{0.562 + 1.4 \cdot \beta}{\beta \cdot (1 + 1.4 \cdot \beta} \right) \tag{A.5}$$

The collisional ionization can be neglected, as its ionization rate coefficient from the level n is much smaller than the radiative decay A_{n_1,n_0} of this level to the ground state. The radiative recombination rate coefficient to the level n is also much smaller than the CX recombination rate $N_H v_H \sigma_n^{CX}$. For the collisional ionization and radiative recombination rate coefficients for the level n, the following formulae [5] are used:

$$\left\langle v\sigma_n^{ion} \right\rangle = 6.0 \cdot 10^{-8} \cdot q \cdot \left(\frac{Ry}{I_Z} \right)^{3/2} \cdot \beta_Z^{\,1/2} \cdot exp(-\beta_Z) f(\beta_Z) \ [\mathrm{cm}^3/\mathrm{s}], \tag{A.6}$$

$$\left\langle v\sigma_n^{rr} \right\rangle = 5.1 \cdot 10^{-14} \cdot Z \cdot \beta_Z^{\,3/2} f(\beta_Z) \quad [\mathrm{cm}^3/\mathrm{s}], \tag{A.7}$$

where q is the number of equivalent electrons on the level n_v (for Hydrogen-like ions q=1), $\beta_Z = I_Z / T_e$ and $I_Z = Ry \cdot (Z/n)^2$ is the corresponding binding energy.

Let us compare the rates (their ratios) of the four processes listed above. In Fig. 12 the ratios of the processes which populate and depopulate the level n_v (for visible domain) of H-like ions of injected impurity with nuclear charge Z are shown for typical plasma parameters T_e = 2 keV and $N_e = 3 \cdot 10^{13}$ cm^{-3}. It is seen that all ratios are rather small, which allows us to neglect the corresponding processes in the simplified form of CR set of equations.

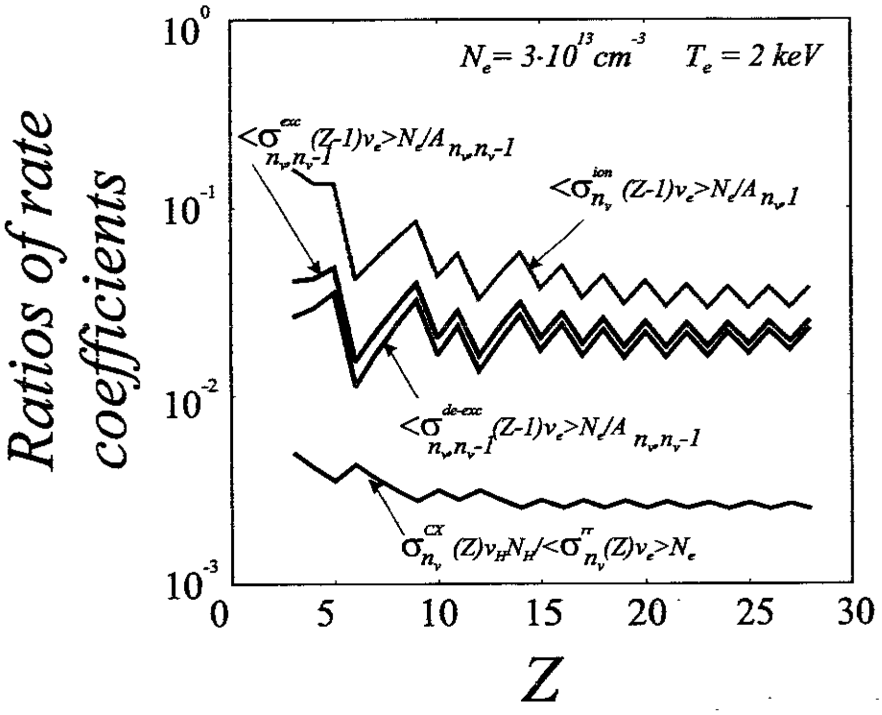

Fig. 12. *The ratios of different processes that populate and depopulate the level n_v versus charge of injected impurity Z for typical plasma parameters in LHD.*

For calculations of the simplified ionization balance, we should use the effective (total) rate coefficients of ionization of H- and He-like ions, radiative recombination of the nuclei, H-like ions and dielectronic recombination of H-like ions.

Results of calculations of effective ionization rate coefficients of H -like ions performed by the CR model [5] confirm that they are rather close to those calculated by Eq. (A.6) with $n_v = 1$.

For the total rate coefficient of radiative recombination of impurity nuclei with charge Z, the formula from Ref. [11] was used:

$$\left\langle v\sigma_{tot}^{rr}(Z)\right\rangle = 5.18\cdot 10^{-14}\cdot Z\cdot \xi_z\cdot f_1(\xi_z) \qquad [\mathrm{cm^3/s}], \qquad (A.8)$$

$$\xi_z = Z/137\cdot(500/T_e^{1/2}(eV))$$

$$f_1(\xi_z) = \ln(\xi_z) + 0.45 + \frac{0.463}{\xi_Z^{2/3}} + \frac{0.067}{\xi_Z^{4/3}} + \frac{0.078 - 0.046\cdot\ln(\xi_z)}{\xi_Z^2}.$$

To calculate the total rate coefficient of radiative recombination of H-like ions we used Eq. (A.8) with charge *Z-1*. Accuracy of about 50% was found for this approach by comparing the results of accurate calculations of these rate coefficients [10] with the $\left\langle v\sigma_{tot}^{rr}(Z-1)\right\rangle$ values obtained from Eq. (A.8).

The rate coefficient for dielectronic recombination from H-like ions to He-like ions was taken from the Ref. [12]:

$$\left\langle v\sigma^{dr}(Z)\right\rangle = 2.7\cdot 10^{-9}\cdot\frac{A_1(Z)}{(T_e(eV))^{3/2}}\cdot\exp\left(-\frac{A_2(Z)}{T_e(eV)}\right)\cdot\exp(-A_3(Z)) \qquad [\mathrm{cm^3/s}], \quad (A.9)$$

$$A_1(Z) = \frac{1230}{Z^{0.14}}\cdot\exp\left(-\frac{44}{Z+2.86}\right), \quad A_2(Z) = 7.5\cdot Z^2, \quad A_3(Z) = 0.0222\cdot Z$$

Recent Issues of NIFS Series

NIFS-684	S Kida and S Goto, Line Statistics Stretching Rate of Passive Lines in Turbulence Mar 2001
NIFS-685	R Tanaka, T Nakamura and T Yabe Exactly Conservative Semi-Lagrangian Scheme (CIP-CSL) in One-Dimension Mar 2001
NIFS-686	S Toda and K. Itoh, Analysis of Structure and Transition of Radial Electric Field in Helical Systems Mar 2001
NIFS-687	T Kuroda and H Sugama, Effects of Multiple-Helicity Fields on Ion Temperature Gradient Modes Apr 2001
NIFS-688	M Tanaka, The Origins of Elctrical Resistivity in Magnetic Reconnection Studies by 2D and 3D Macro Particle Simulations Apr 2001
NIFS-689	A Maluckov, N Nakajima, M Okamoto, S Murakami and R Kanno, Statistical Properties of the Neoclassical Radial Diffusion in a Tokamak Equilibrium Apr 2001
NIFS-690	Y Matsumoto, T Nagaura, Y Itoh, S-I Oikawa and T Watanabe, LHD Type Proton-Boron Reactor and the Control of its Peripheral Potential Structure Apr 2001
NIFS-691	A Yoshizawa, S -I Itoh, K Itoh and N Yokoi, Turbulence Theories and Modelling of Fluids and Plasmas Apr 2001
NIFS-692	K Ichiguchi, T Nishimura, N Nakajima, M Okamoto, S -i. Oikawa, M Itagaki, Effects of Net Toroidal Current Profile on Mercier Criterion in Heliotron Plasma Apr 2001
NIFS-693	W Pei, R Horiuchi and T Sato Long Time Scale Evolution of Collisionless Driven Reconnection in a Two-Dimensional Open System. Apr 2001
NIFS 694	L N Vyachenslavov, K Tanaka, K Kawahata, CO2 Laser Diagnostics for Measurements of the Plasma Density Profile and Plasma Density Fluctuations on LHD Apr 2001
NIFS-695	T Ohkawa, Spin Dependent Transport in Magnetically Confined Plasma May 2001
NIFS-696	M Yokoyama, K Ida, H Sanuki, K Itoh, K Narihara, K Tanaka, K Kawahata, N Ohyabu and LHD experimental group Analysis of Radial Electric Field in LHD towards Improved Confinement May 2001
NIFS-697	M Yokoyama, K Itoh, S Okamura, K Matsuoka, S. -I Itoh, Maximum-J Capability in a Quasi-Axisymmetric Stellarator. May 2001
NIFS-698	S-I. Itoh and K. Itoh, Transition in Multiple-scale-lengths Turbulence in Plasmas May 2001
NIFS-699	K. Ohi, H Naitou, Y. Tauchi, O Fukumasa, Bifurcation in Asymmetric Plasma Divided by a Magnetic Filter: May 2001
NIFS-700	H Miura, T Hayashi and T Sato, Nonlinear Simulation of Resistive Ballooning Modes in Large Helical Device June 2001
NIFS-701	G Kawahara and S Kida, A Periodic Motion Embedded in Plane Couette Turbulence June 2001
NIFS-702	K Ohkubo, Hybrid Modes in a Square Corrugated Waveguide: June 2001
NIFS-703	S -I Itoh and K Itoh, Statistical Theory and Transition in Multiple-scale-lengths Turbulence in Plasmas· June 2001
NIFS-704	S Toda and K. Itoh. Theoretical Study of Structure of Electric Field in Helical Toroidal Plasmas. June 2001
NIFS-705	K. Itoh and S-I. Itoh, Geometry Changes Transient Transport in Plasmas June 2001
NIFS-706	M Tanaka and A Yu Grosberg Electrophoresis of Charge Inverted Macroion Complex Molecular Dynamics Study July 2001
NIFS-707	T-H Watanave, H Sugama and T Sato A Nondissipative Simulation Method for the Drift Kinetic Equation July 2001
NIFS-708	N Ishihara and S Kida, Dynamo Mechanism in a Rotating Spherical Shell Competition between Magnetic Field and Convection Vortices July 2001
NIFS-709	LHD Experimental Group, Contributions to 28th European Physical Society Conference on Controlled Fusion and Plasma Physics (Madeira Tecnopolo, Funchal, Portugal, 18-22 June 2001) from LHD Experiment: July 2001
NIFS-710	V Yu Sergeev, R K Janev, M J Rakovic, S. Zou N Tamura, K V Khlopenkov and S Sudo Optimization of the Visible CXRS Measurements of TESPEL Diagnostics in LHD, Aug 2001